Ultra-Sensitive, Durable and Stretchable Ionic Skins with Biomimetic Micronanostructures for Multi-Signal Detection, High-Precision Motion Monitoring, and Underwater Sensing

Lili Ma,[a] Jiaxin Wang,[a] Jinmei He,*[a] Yali Yao,[a] Xuedan Zhu,[a] Lei Peng,[a] Jie Yang,[b] Xiangrong Liu,[a] and Mengnan Qu*[a]

* Corresponding authors: *mnanqu@gmail.com*; *jinmhe@gmail.com*.

[a] College of Chemistry and Chemical Engineering, Xi'an University of Science and Technology, Xi'an 710054, China

[b] College of Safety Science and Engineering, Xi'an University of Science and Technology, Xi'an, 710054, China

Supporting Information

Experimental Section

1. Fabrication of the Amino Modified HNTs (mHNTs). Firstly, the HNTs were treated by alkaline to increase the hydroxyl active sites on its surface. Specifically, 3 g HNTs were slowly added in a 200 mL alkaline (pH = 12) aqueous solution, then ultrasonically dispersed for 30 min and stirred at 60 °C for 5 h. Later on, the obtained alkaline-treated HNTs were separated from the mixed solution by centrifuge and repeatedly washed by deionized water until the pH decreased to 7, then dried at 60 °C for 12 h and grinded into powders.

Secondly, the above alkaline-treated HNTs (2 g) were ultrasonically dispersed in 40 mL ethanol and stirred at 60 °C until the mixture mixed completely, then adding 0.5 g APTES into the mixture and continually stirring at 60 °C for 5 h. The mHNTs was obtained after washing, suction filtrating, drying, and grinding.

2. Fabrication of the Superhydrophobic VHB Layer. 0.5 g uncured PDMS solution (PDMS prepolymer and curing agent mixed with a weight of 9:1) was added to 50 mL of n-hexane and stirred until the components were completely mixed. Then, 0.2 g nanoscaled SiO_2 was dispersed in the mixed solution and stirred at room temperature for later use. Later on, the as-prepared SiO_2/PDMS mixed solution was sprayed onto a VHB substrate with a tensile strain of 300% in the horizontal axis (X-axis) direction. Then, symmetrical release along the X-axis direction made the substrate strain shrink back to about 10%, and curing the substrate at 60 °C for 15 min. Thereafter, the VHB substrate returned to its original shape and further

washed in ethanol to remove the redundant SiO_2 particles and dried. Finally, the VHB substrate with excellent surface superhydrophobicity was obtained.

3. Fabrication of the Array Pressure Sensing Device. For the design of the arrays of the pressure sensors, VHB layer with thickness of 0.5 mm was stacked on a glass substrate (40 mm × 45 mm). Then, four MIS films (13 × 13 mm) were separately stacked on the VHB substrate in a 2 × 2 array, and Cu tapes were put below both sides of each MIS film as electrodes. To establish external contacts, two Cu wires were placed under the two ends of the Cu tapes electrodes. The distance between the adjacent MIS sensors was about 5 mm, and for each MIS sensor, the distance between the adjacent electrodes was about 11 mm. Thereafter, the scotch tape was covered and stacked on the sensor arrays, and then the pressure sensing device was obtained. In addition, the width and length of our device could be adjusted to fit different testing requirements.

4. Characterizations. The surface morphology of the resultant samples were characterized by scanning electron microscopy (SEM, Zeiss Sigma300), the composition and distribution of surface elements of the superhydrophobic VHB sample were measured by energy-dispersive X-ray spectroscopy (EDS, HORIBA 7593-H) attached to SEM. Fourier transform infrared spectroscopy (FTIR, PerkinElmer System 2000) was applied to investigate the surface chemical compositions of the resultant mHNTs. The measurement of the mechanical properties of the obtained samples was carried out by a universal tensile testing machine (MTS CMT6103). Notably, all the tensile testing specimens were cut into strips of 0.5 mm in thickness, 5 mm in width, and 35 mm in length. These samples were subjected to tensile testing with an identical stretching rate of 50 mm/min. Moreover, to evaluate the

compressibility of the samples, the testing specimens were cut into cuboids of 2.5 mm in thickness, 20 mm in width, and 20 mm in length. The compression tests were carried out at 70% strain, and the speed was controlled at 0.2 mm/min. The CAs and SAs were measured with 2.5 µL droplets of water and other liquids using a contact-angle goniometer (JC2000DM, China) at ambient temperature. Noteworthy, the final measurement data was an average of five different spots on the same sample. The temperature variations of the MIS-based sensors were characterized via using an UTi260B 9 Hz thermal imager. The resistance and electrical conductivities of the obtained samples were measured through two-probe resistance tester on the digit graphical sampling multimeter with a resistance of 10 MΩ (DMM6500 6 1/2, Keithley, USA).
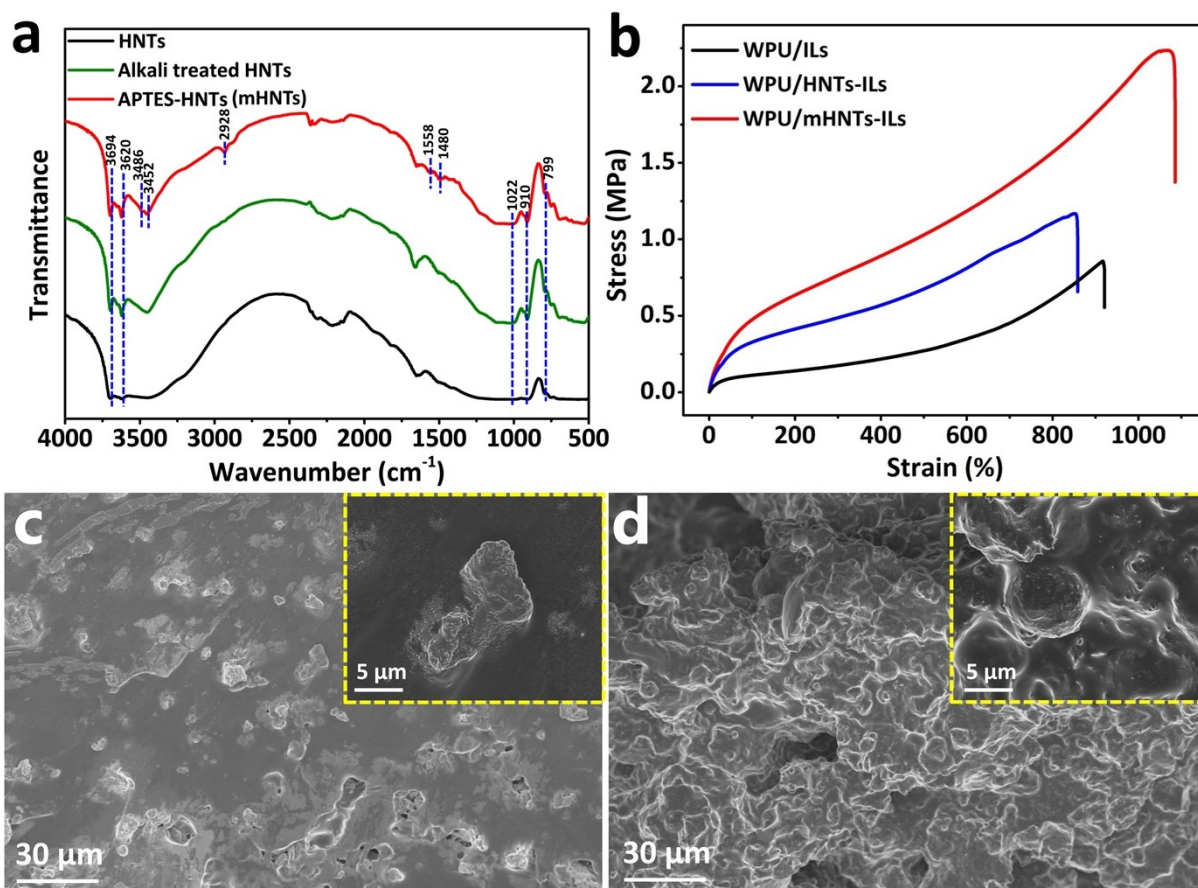
Fig. S1 (a) FTIR spectra of the original HNTs, alkali treated HNTs, and the APTES functionalized HNTs (mHNTs), respectively. (b) Stress-strain curves of the ionogel samples containing HNTs and mHNTs respectively. (c,d) SEM images of the fracture surface morphologies of the two ionogel samples containing HNTs (c) and mHNTs (d) respectively. The images with yellow border are the enlarged images of the corresponding samples' morphologies.

Fig. S1 shows the FTIR spectra of the HNTs in different conditions. For pristine HNTs, the stretching vibration peaks locating at 3694 cm^{-1} and 3620 cm^{-1} and are assigned to −OH groups on HNTs surfaces. Moreover, the peak at 910 cm^{-1} is bending vibration of −OH groups. The vibration peak at 1022 cm^{-1} is assigned to Si−O bonds, while the peak at 799 cm^{-1} is ascribed to symmetrical stretching vibration of Si−O−Si. After the treatment of alkali, the adsorption peaks of −OH groups at 3694 cm^{-1}, 3620 cm^{-1}, 910 cm^{-1}, and 610 ~ 690 cm^{-1} become intensified, indicating the increase of the hydroxyl active sites on the HNTs surface.

In this case, when the alkali treated HNTs is further functionalized by APTES, several new absorption peaks appear on the m-HNTs surfaces. Two new peaks emerged at 3486 cm^{-1} and 3452 cm^{-1} are ascribed to the $-NH_2$ groups, and the peak discovered around 1558 cm^{-1} is corresponded to the bending vibration of N−H in $-NH_2$ groups. The additional vibration peaks at 2928 cm^{-1} and 1480 cm^{-1} are assigned to symmetrical stretching vibration of C−H in $-CH_2-$ groups and bending vibration of C−H bonds. All these results confirmed that the APTES is successfully grafted on the functionalized m-HNTs surfaces, contributing to a high dispersing ability of the m-HNTs in WPU polymer matrix.

To investigate the compatibility of mHNTs with ionogel matrix, the addition of the HNTs and mHNTs on mechanical property of the ionogel has been further tested. As shown in Fig. S1b, the addition of the mHNTs greatly improves the mechanical strength of the original ionogel (WPU/ILs). Comparing with the WPU/HNTs-ILs ionogel, the WPU/mHNTs-ILs ionogel exhibits more superior mechanical property with a tensile strength of 2.28 MPa and an elongation rate of 1090.5%. This result indicates that after the surface treatment, the bonding strength between the resulted mHNTS and WPU matrix is significantly enhanced. The addition of the HNTs increases the mechanical strength of the original ionogel while the elongation at break is decreased, which may be ascribed to the uneven distribution of HNTs in the ionogel matrix. To further confirm this hypothesis, the fracture surface morphologies of the WPU/HNTs-ILs ionogel and WPU/mHNTs-ILs ionogel are investigated. As shown in Fig. S1c, the fracture surface of the WPU/HNTs-ILs ionogel is relatively flat, and it can be observed that the HNTs are agglomerated in the matrix and distributed unevenly. The results show that the interfacial adhesion between unmodified HNTs and WPU matrix is not strong

enough, thus the mechanical enhancement effect on the ionogel is not obvious. Different from the morphology in Fig. S1c, it can be observed in Fig. S1d the fracture surface morphology of the WPU/HNTs-ILs ionogel is relatively rough. Moreover, the enlarged morphology image demonstrates that the mHNTs are uniformly and homogeneously distributed in the WPU matrix, which is due to the decrease of van der Waals force of the mHNTs, thus reducing their agglomeration in the matrix. Meanwhile, the aminopropyl groups on the mHNTs surfaces can form a strong chemical bond with the WPU, which greatly improves the compatibility between mHNTs and WPU matrix. The coexistence of chemical bonding and mechanical bonding between the mHNTs and the WPU polymer has qualitatively improved the mechanical properties of the resulted ionogel.
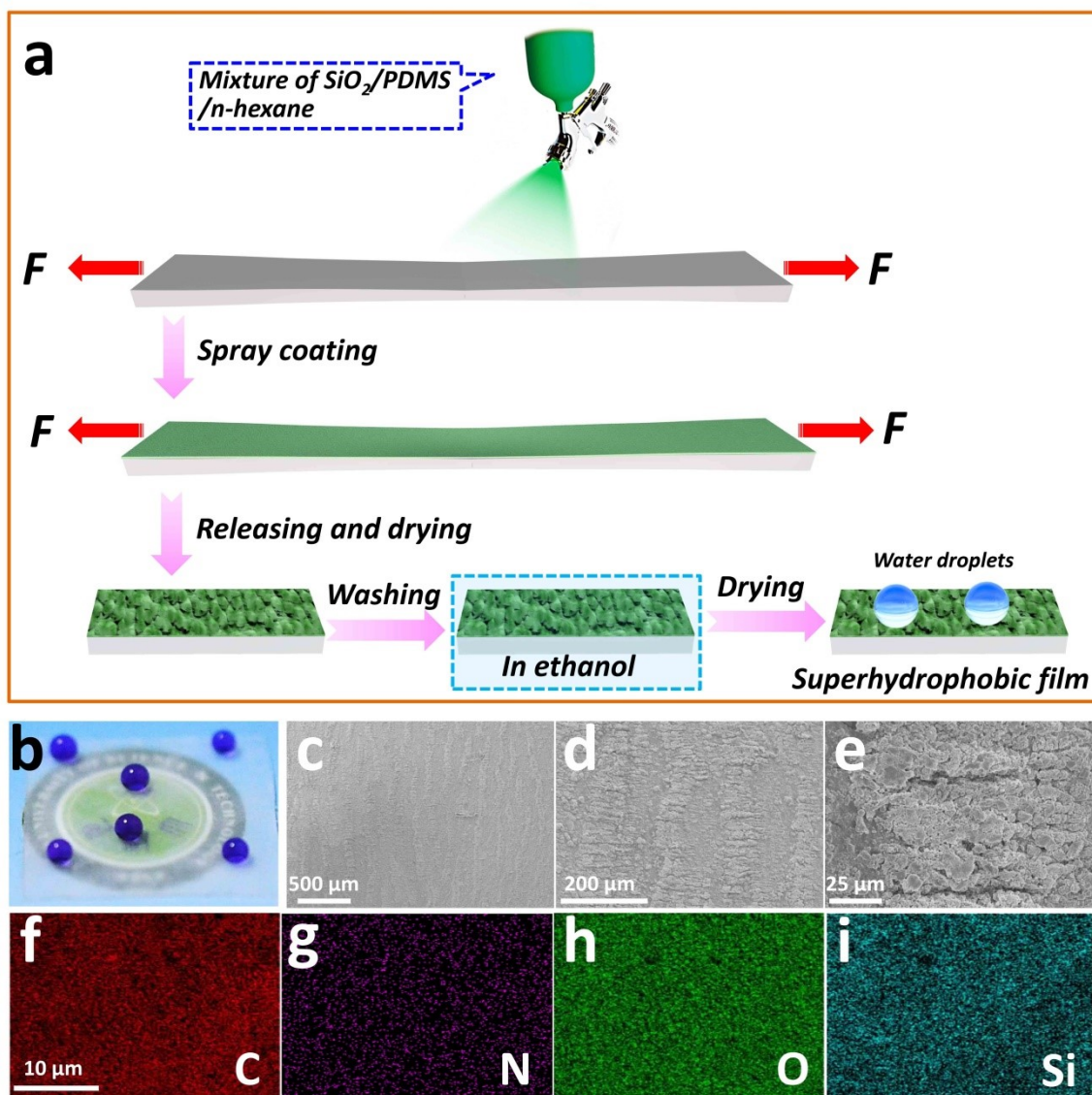
Fig. S2 (a) Fabrication of the superhydrophobic VHB layer. (b-i) Photograph of the superhydrophobic VHB layer (b) and its SEM (c-e) and EDS mapping images (f-i).

The schematic illustration of fabricating the superhydrophobic VHB layer is shown in Fig. S2a. The SiO_2/PDMS/n-hexane suspension is sprayed onto a VHB substrate with a tensile strain of 300% in horizontal axis (x-axis) direction. Then, the symmetrical release along the X-axis direction makes the VHB substrate strain shrink back to about 10%, and then the VHB layer is dried at 60 °C for 15 min. Afterwards, the VHB substrate is restored to its original shape, and then washed in ethanol to remove the redundant SiO_2 particles and dried. As a

result, a VHB layer with excellent surface superhydrophobicity is obtained. As exhibited in Fig. S2b, the resultant superhydrophobic VHB layer preserves good transparency and shows favourable water repellency. The special surface superwettability is mainly related to the surface structure and chemical composition of the as-obtained VHB substrate. Therefore, the micromorphology of the superhydrophobic VHB layer is characterized via using SEM. As shown in Fig. S2c-e, the surface-modified VHB substrate exhibits a micro-wrinkle surface structure, which is important for the construction of superwettable surface. In addition, the surface elements of the superwettable VHB layer are corroborated by elemental mapping as shown in Fig. S2f-i. The results imply that after the modification of the SiO_2/PDMS, elements C, N, O, and Si are uniformly distributed on the VHB substrate surface, thus endowing the surface with excellent hydrophobicity.
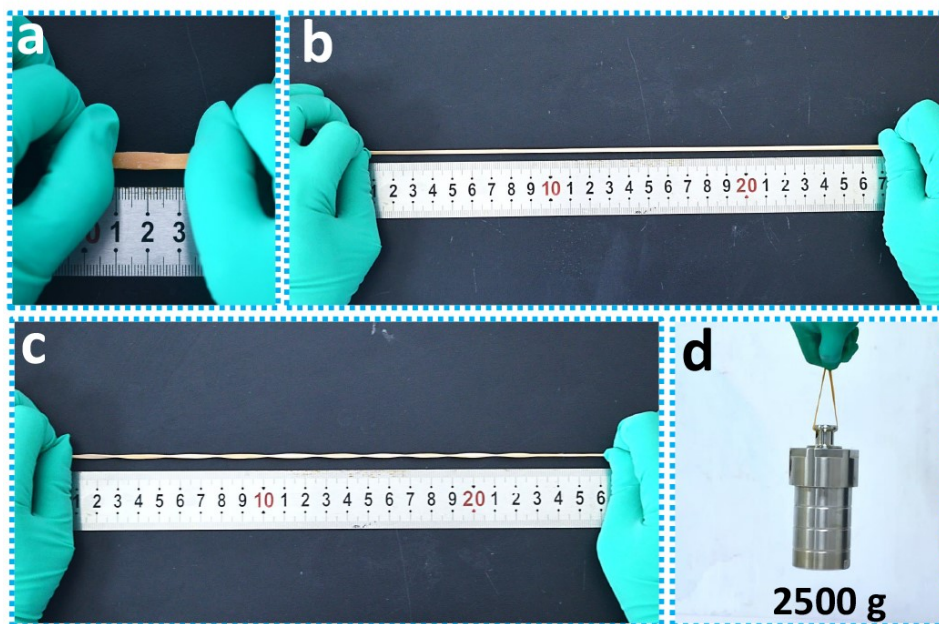
Fig. S3 Mechanical properties of the WPU/mHNTs-ILs ionogels. (a-c) Photographs showing the excellent stretching (a,b) and stretching-twisting (c) flexibility of the WPU/mHNTs-ILs ionogel. (d) Load-bearing capacity of the WPU/mHNTs-ILs ionogel.
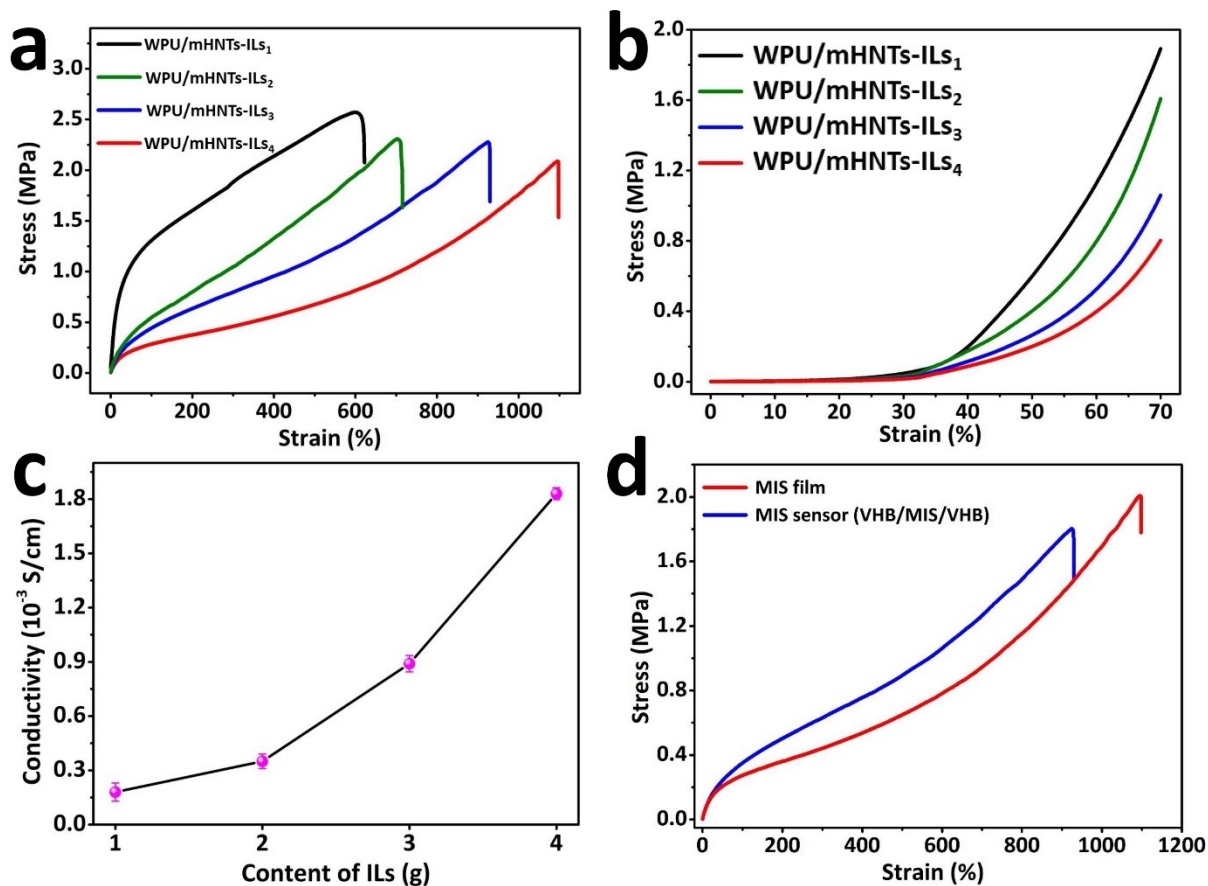
Fig. S4 (a,b) Stress-strain curves (a) and compression curves (a) of the WPU/mHNTs-ILs ionogels with different ILs contents. (c) Conductivities of the WPU/mHNTs-ILs ionogels with different ILs contents. (d) Stress-strain curves of the MIS-based sensor.

The mechanical properties and conductivities of the WPU/mHNTs-ILs ionogels are significantly influenced by the ILs. To determine the optimum content of the ILs in WPU/mHNTs-ILs ionogel, the mechanical properties and conductivities of the ionogels with different IL contents (1 g (IL_1), 2 g (IL_2), 3 g (IL_3), 4 g (IL_4)) have been further characterized, wherein the contents of WPU and mHNTs maintain at 10 g and 0.8 g, respectively. As shown in Fig. S4a, with the increase of IL content, the tensile strength of the WPU/mHNTs-ILs ionogel gradually decreases while the corresponding stretchability is significantly improved. Moreover, the compression properties present the similar trends (Fig. S4b). These results are attributed to that a higher content of IL leads to a lower density of the polymer networks, and

finally a decrease in mechanical strength. On the other hand, the ILs can form strong dynamic hydrogen bonding with the polymers as well as the mHNTs, which can not only separate the joint points of the polymeric chains but also be possible to make the mHNTs uniformly disperse in the polymer matrix. Moreover, these dynamic hydrogen bonds in the ionogel can facilitate the unfolding and sliding of the polymeric chains during deformation by continuously breaking and reforming. As a result, the stretchablility of the WPU/mHNTs-ILs ionogel increases as the content of the ILs increases. Remarkably, as the content of the ILs attains to 4 g, the resultant ionogel shows better synthetical mechanical properties. It can be ascribed to the strong hydrogen bond interactions and good compatibility of the ILs, mHNTs, and WPU polymeric chains in the ionogel. In addition, for all of the WPU/mHNTs-ILs ionogels, the ionic conductivity increases as the content of ILs increases (Fig. S4c). As the content of ILs increases from 1 g to 4 g, the conductivity of the resulted ionogel at room temperature increases from 0.18×10^{-3} to 1.85×10^{-3} S/cm. This can be due to the fact that an increase of the ILs content results in an increase in the concentration of mobile ions and a decrease in the density of the polymer networks as well as an increase in free volume, all of which promote the movement of ILs. In addition, the above results suggest that the optimum content of ILs in the WPU/mHNTs-ILs ionogel is about 4 g as the contents of WPU and mHNTs maintain at 10 g and 0.8 g. Therefore, the ionogel (MIS) samples that tested and discussed in the manuscript are all prepared in this proportion. Besides, with the MIS film as the ionic conductor, and two layers of VHB substrate as the protective layers, a MIS-based sensor is obtained. As shown in Fig. S4d, both the MIS film and the resultant MIS sensor are

highly stretchable, and the obtained MIS sensor shows an excellent strechability with a tensile
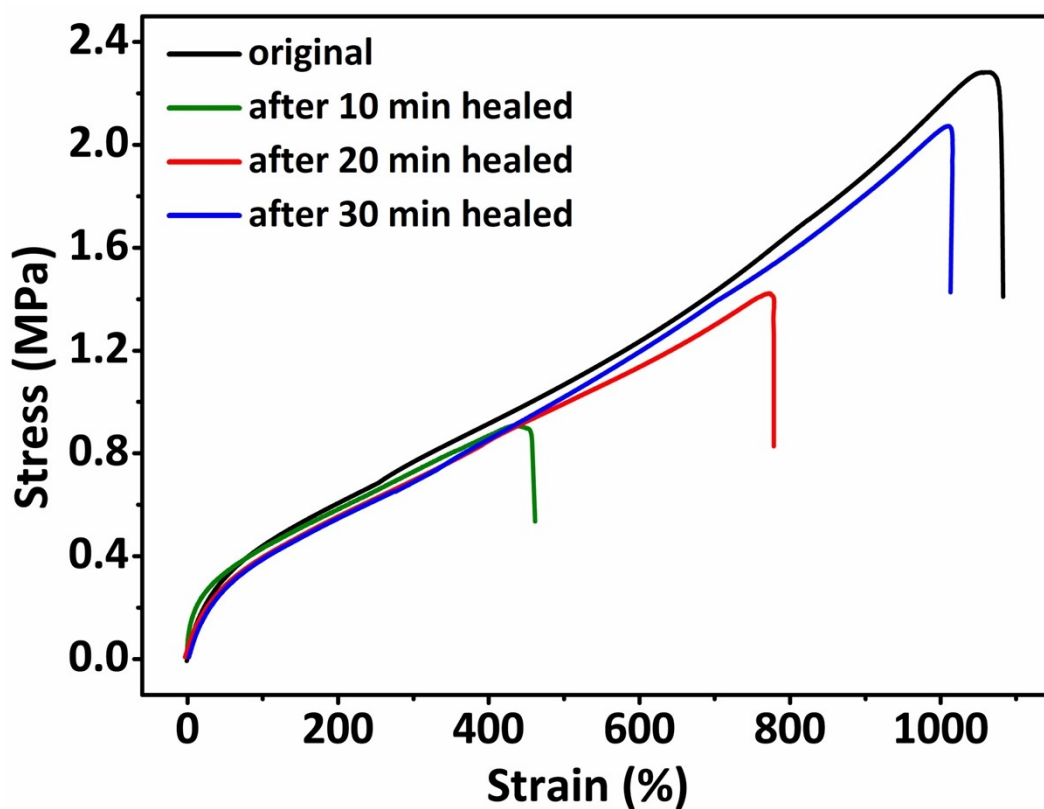
strength of 1.85 MPa and a strain at break about 940%.

Fig. S5 Stress–strain curves of the original WPU/mHNTs-ILs ionogel and the WPU/mHNTs-ILs ionogel

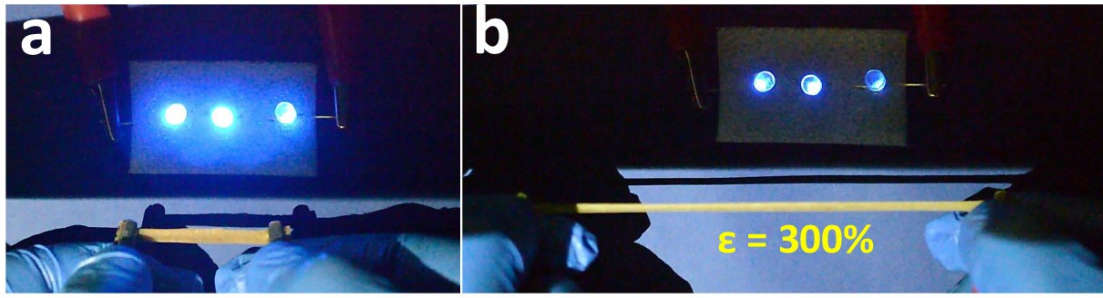previously cut into two halves and healed for 10, 20, and 30 min.

Fig. S6 (a,b) The LED brightness changes under different elongations (0% and 300%) of the MIS film.
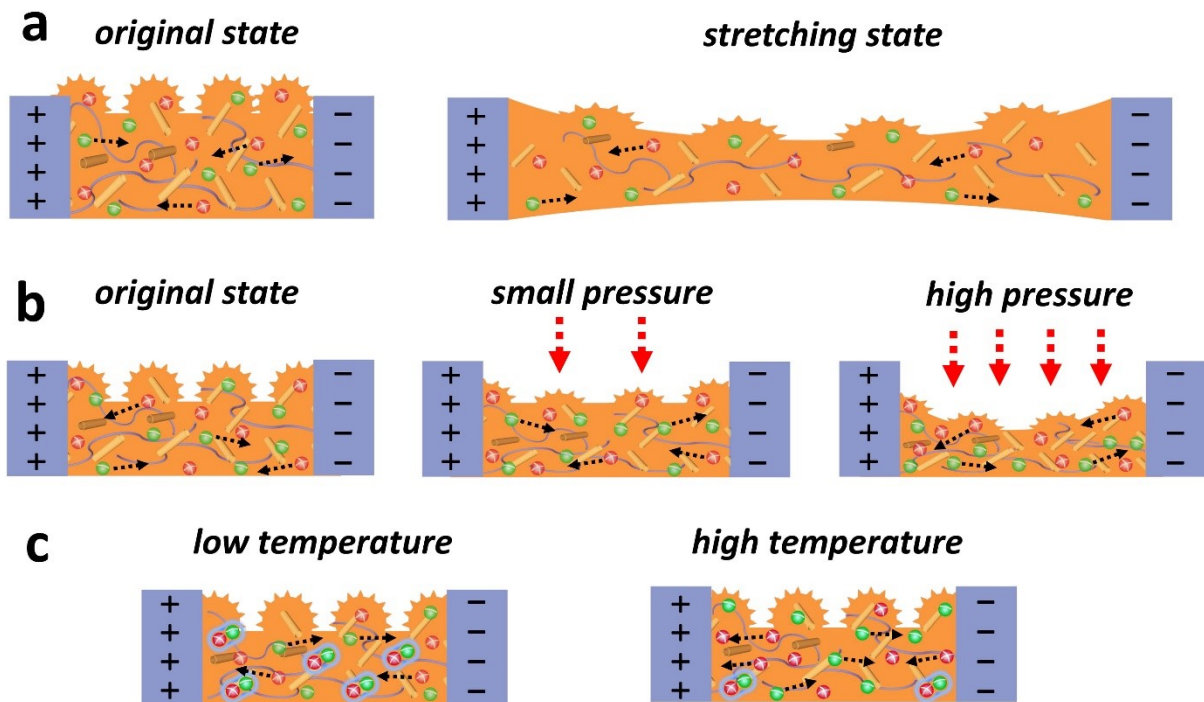

Fig. S7 Schematic illustration of the (a) strain sensing mechanism, (b) pressure sensing mechanism, and (c) temperature sensing mechanism of the MIS based sensor.
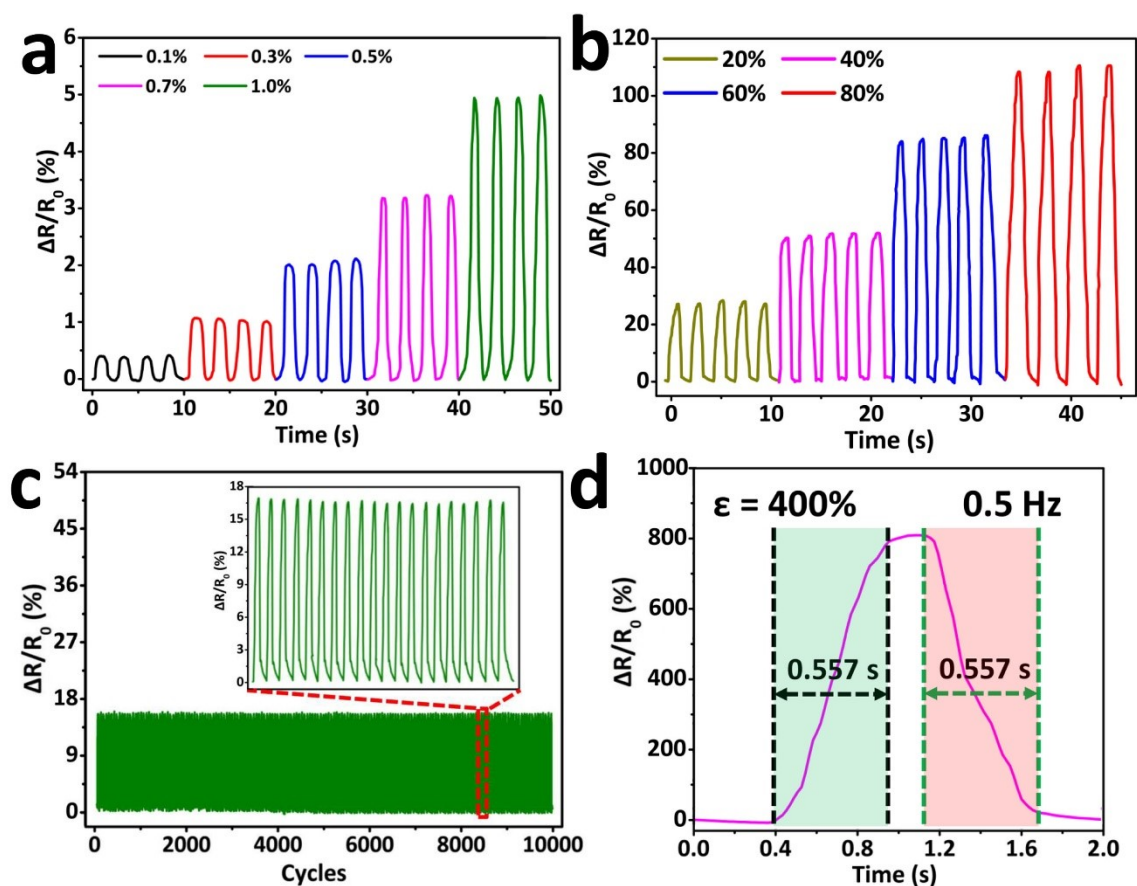
Fig. S8 (a,b) Relative resistance changes of the MIS-based sensors under an extremely small strain range (a) and a relative large strain range (b). (c) Cyclic stability tests of the MIS-based sensors under 10% strain for 10000 cycles. (d) Measurement of the response time and recovery time of the MIS-based sensor under a strain of 400% (0.5 Hz) after the sensor experienced 5000 extension-release cycles at 400% strain.
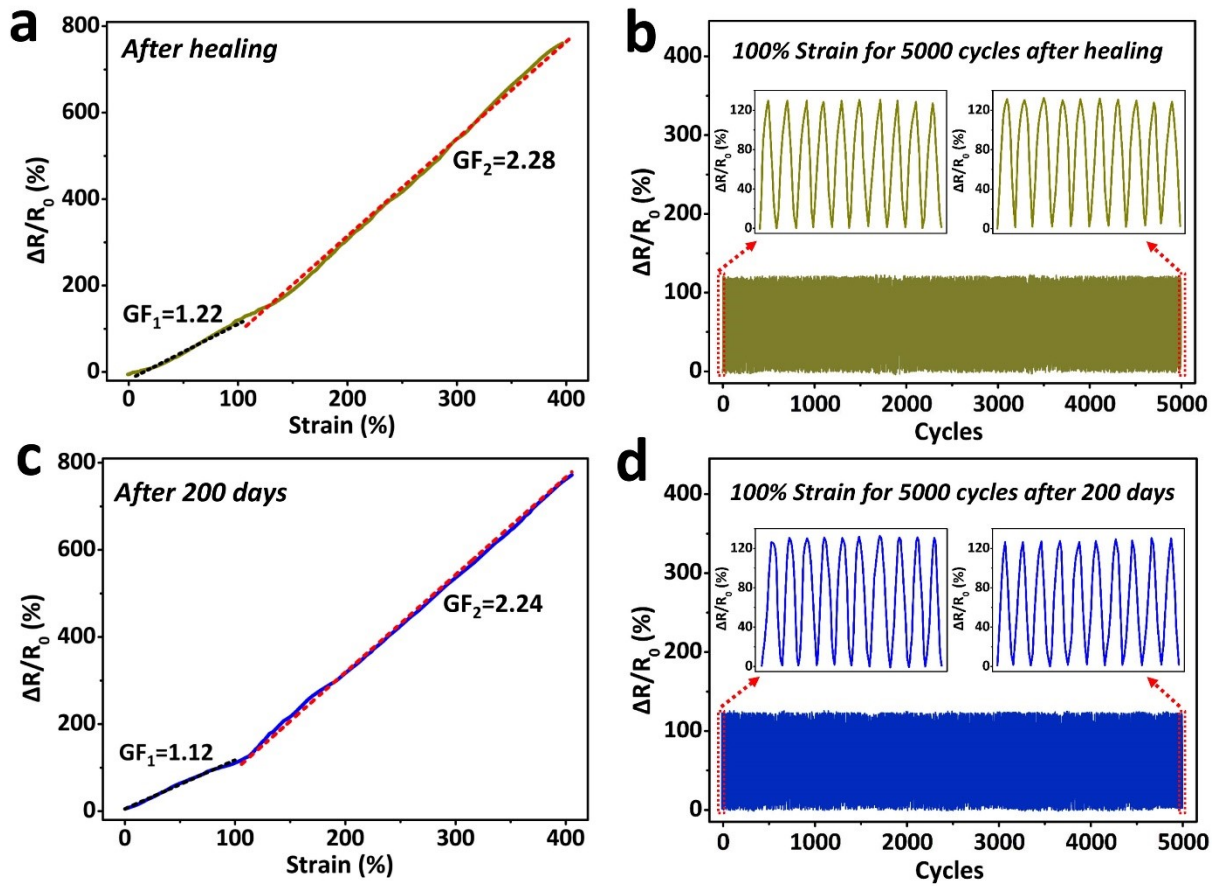
Fig. S9 (a) Relative resistance changes of the healed MIS-based sensors a function of strain. (b) Cyclic stability tests of the healed MIS-based sensor under 100% strain for 5000 cycles. (c) Relative resistance changes of the MIS-based sensor after being stored in open air for 200 days as a function of strain. (d) Cyclic stability test of the MIS-based sensor after being stored in open air for 200 days under 100% strain for 5000 cycles.
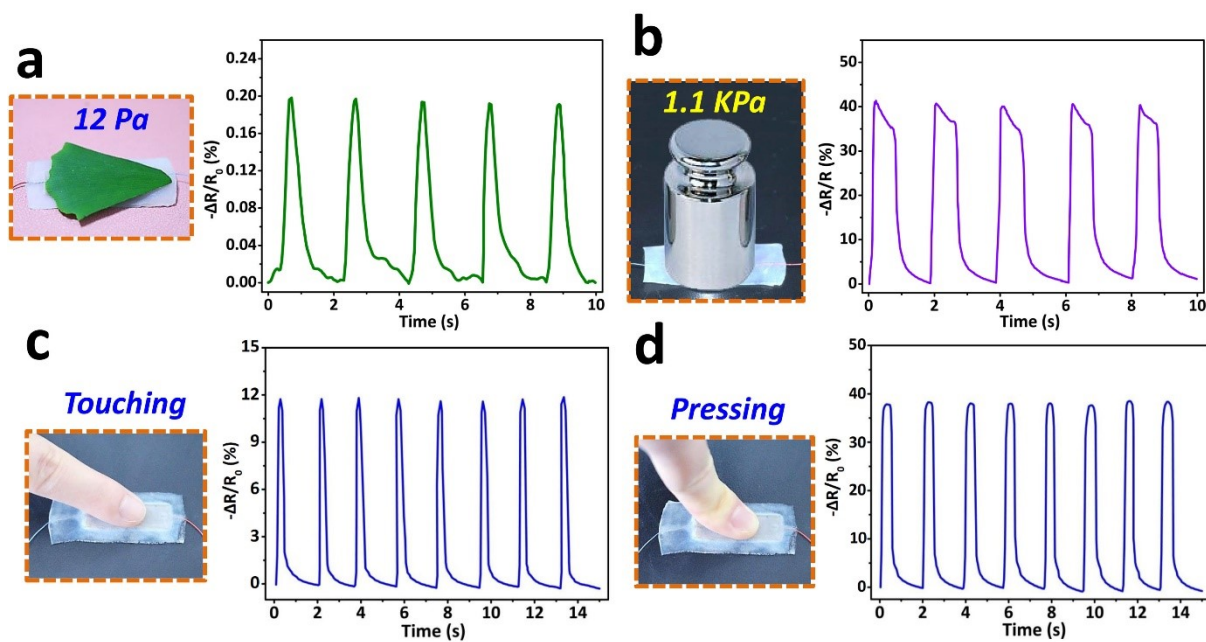
Fig. S10 Relative resistance variation responses of the MIS-based sensor for sensing and detecting various types of pressure, including subtle pressure of the light ginkgo leaf (12 Pa) (a), high pressure of a 500 g weight (1.1 KPa) (b), as well as the pressures caused by human finger touching (c) and pressing (d), respectively.
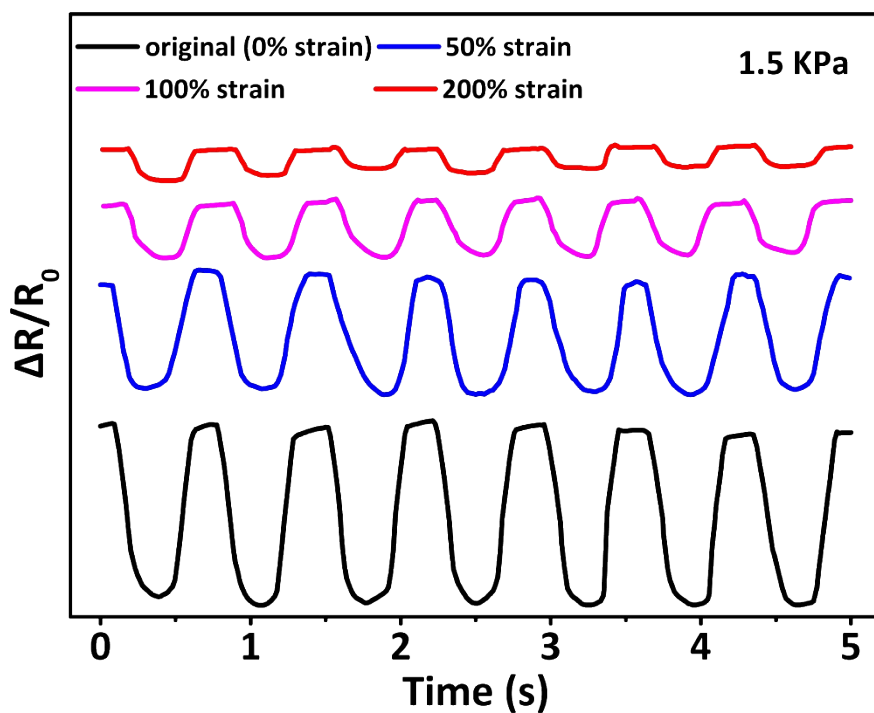

Fig. S11 Relative resistance changes with different strains (0%, 50%, 100%, and 200%) under a constant pressure of 1.5 KPa.
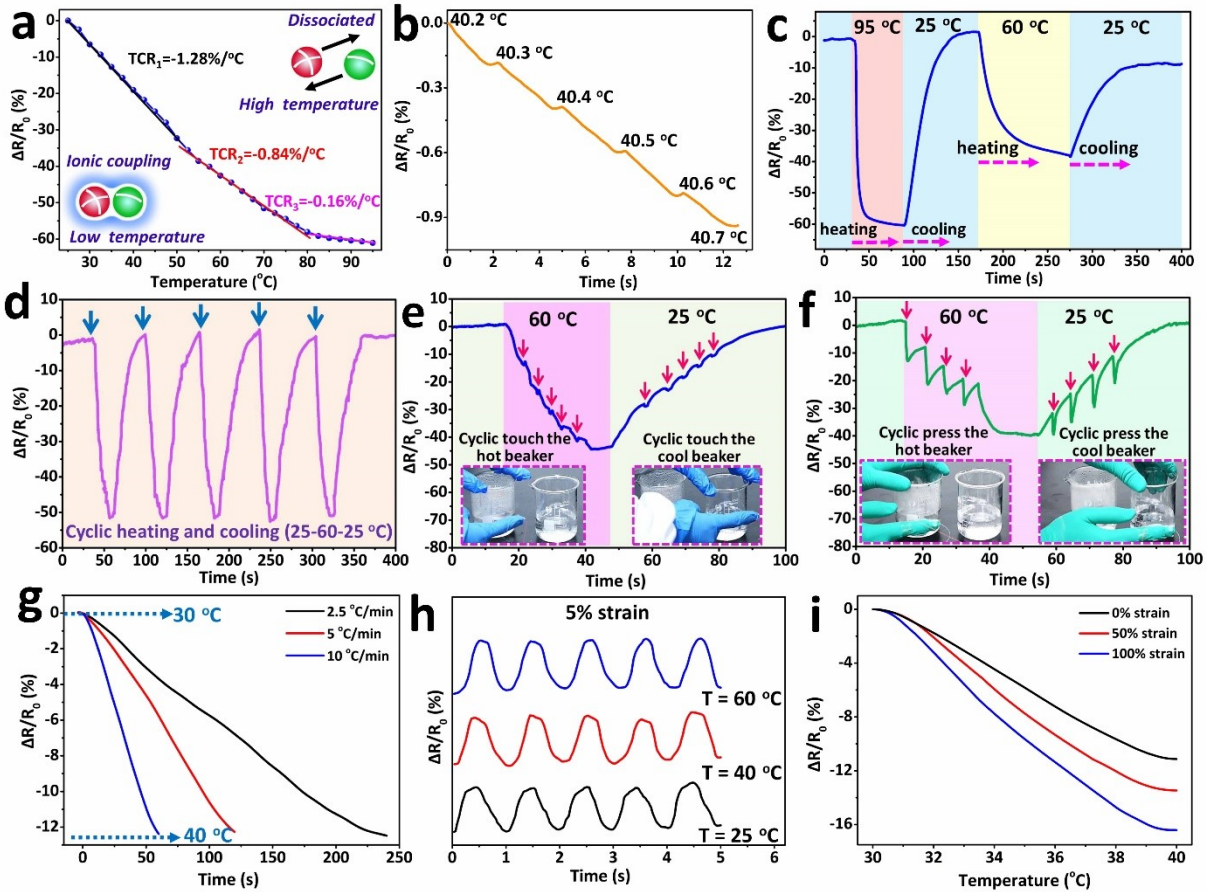
Fig. S12 (a) Relative resistance changes of the MIS-based sensor with increasing temperature. (b) Variation in relative resistance as increasing the temperature from 40.2 to 40.7 °C with a temperature gradient of 0.1 °C. (c) Variation in relative resistance when the MIS sensor is separately heated and cooled at different temperature (95–25–60–25 °C). (d) Variation in relative resistance as the MIS sensor is cyclically heated and cooled between 25 and 60 °C. (e,f) Variation in relative resistance when the finger attached with the MIS sensor continuously touches and moves away from hot (60 °C) and cool (25 °C) water beakers (e) and continuously presses and moves away from hot (60 °C) and cool (25 °C) water beakers (f). (g) Relative resistance changes with different heating rates under a constant temperature gradient of 10 °C. (h) Relative resistance changes with different temperatures under a constant strain of 5%. (i) Relative resistance changes with temperature under different strains at a constant temperature gradient of 10 °C.

Since the electrical conductivity of the MIS relies on the free migration ions in its matrix, the ion mobility of free ions increases with the increase of temperature, which results in an increase in conductivity and a decrease in resistance accordingly.[21,22] Therefore, the MIS

shows an interesting temperature-dependent ionic conductivity and can be applied as temperature sensors to mimic the response of environmental temperature change on the human skin. To demonstrate this hypothesis, the relative resistance variation ($\Delta R/R_0$) of the MIS-based sensor with respect to the temperature range of 25 to 95 °C is shown in Fig. S12a. The slope of the resulted curve represents the temperature sensitivity of the sensor, and the temperature coefficient of resistance (TCR) is defined as TCR = $(R-R_0)/R_0/(T-T_0)$ = $\Delta R/R_0/(T-T_0)$, wherein R and R_0 are the instantaneous resistance at a particular temperature T and reference temperature T_0 (25 °C), respectively. It can be found that the ratio of ($\Delta R/R_0$) decreases as the temperature elevates from 25 °C to 95 °C, which is consistent with the results reported in previous work.[23,24] Moreover, the absolute value of TCR ranges from 1.28%/°C to 0.16%/°C, which is relatively higher than the most of reported resistance–temperature sensors.[25,26] Specifically, the MIS sensor shows an optimal temperature sensitivity in the range of 25–50 °C (TCR = − 12.8/°C), which is suitable to monitor the changes of body temperature and ambient temperature. As exhibited in Fig. S12b, the MIS sensor can detect a slight temperature change of 0.1 °C, demonstrating a higher detection accuracy, which is helpful to obtain accurate temperature information. In light of the fascinating temperature sensing property, the MIS-based temperature sensor is utilized as bionic i-skin to sense different temperatures (95–25–60–25 °C), so that to evaluate its thermal response performance. As shown in Fig. S12c, the signals of ($\Delta R/R_0$) decrease immediately once the MIS sensor is heated at high temperature (such as 95 °C and 60 °C). However, when it is cooled at ambient (25 °C) temperature, the signal of ($\Delta R/R_0$) firstly keeps decreasing for a few seconds owing to the absorbed heat in MIS sensor cannot be quickly dissipated, and then increases slowly and

returns its original states. Moreover, the signal intensity of the ($\Delta R/R_0$) generated at 95 °C is obviously greater than that at 60 °C due to the higher temperature can effectively improve the ion migration rate in the ionogel, which leads to a significant decrease in resistance. Fig. S12d shows the repeatability and stability of the temperature sensing performance of the MIS sensor, from which it can be found the variation of $\Delta R/R_0$ keeps nearly constant when the temperature is cyclically switched between 25 and 60 °C, exhibiting stable and repeatable temperature sensing performances.

By virtue of the prominent temperature sensing performance, we further attach the MIS sensor, serving as a wearable electronic device, to a human finger to demonstrate its potential application. As shown in Fig. S12e, a continuous touching and moving away process is studied to evaluate the performance of the MIS sensor in the real working status (First: the finger attached with MIS sensor touches and moves away from hot beaker (60 °C) five times in same intervals; Second: keeping touching for seconds; Third: touching and moving away from cool water (25 °C) five times in same intervals, the specific process is shown in Video S2). It can be found during the cycles for continuous touching and moving away from hot baker, the ($\Delta R/R_0$) signal of the MIS sensor decreases with the temperature increasing. The absorbed heat can cause the ($\Delta R/R_0$) signal to continuously decrease after the sensor moving away from hot beaker. More importantly, the ($\Delta R/R_0$) signal has a significant fluctuation as the moment of the finger touches hot beaker, which can be attributed to the combined effect of temperature and pressure strain generated at this moment. There are three abrupt changes of the ($\Delta R/R_0$) signal, which is consistent with the number of touching and moving away from hot beaker. During the sustained touching process because the temperature of the MIS sensor

keeps constant when being close to the hot beaker, the ($\Delta R/R_0$) signal maintains stable without changes. When the MIS sensor touches the cool water, the electrical signals increase immediately. Meanwhile, there are also five abrupt changes of the ($\Delta R/R_0$) signal for touching and moving away from cool water, which is similar to that in the case of hot water. And after five cycles, the value of ($\Delta R/R_0$) almost returns to the original state. In order to further demonstrate the identification property of the MIS as bionic i-skin, we utilize the finger attached with the MIS sensor to cyclically pressing the two beakers mentioned above instead of touching them lightly (Fig. S12f and Video S3), to mimic a double stimuli response of temperature and stress simultaneously applied on the MIS sensor. As a result, it can be observed that despite the variation trend of electrical signals are substantially similar to that in Fig. S12e, when the finger with MIS sensor presses and moves away from the hot beaker, the electrical signal is completely different from before, which consists of an obvious peak signal and a platform signal. The peak signal represents the compressive stress change and the platform signal corresponds to the temperature variation before and after contacting the hot beaker. When the finger presses the hot beaker, the sensor responds to the stress firstly and shows a significant peak signal accordingly. And then, due to the heat absorbing from the hot beaker, the temperature of the sensor increases, inducing lower electrical signal, reflected as a platform signal. More importantly, when the temperature of MIS sensor is close to the cool beaker, the MIS sensor responds not to the temperature of the hot beaker but to the stress, showing excellent identification performance. All these results demonstrate the excellent sensitive response abilities and identification properties of the MIS-based sensor to the

superimposed stimulus of temperature and pressure, which is of great potential for next generation of bionic electronic skin.

In addition, repeatability and stability of the temperature sensing behaviors are important for the MIS sensor. As exhibited in Fig. S12g, when the temperature rises from 30 to 40 °C at different rates (2.5, 5, and 10 °C/min), the variation of ($\Delta R/R_0$) signal remains constant, revealing the excellent reliability and electrical stability of the MIS sensor. Moreover, the strain sensing performance of the MIS sensor under 5% strain at different temperatures (25, 40 and 60 °C) are also investigate. The variation of ($\Delta R/R_0$) signal of the MIS sensor at the above different temperature are approximately the same (Fig. S12h), which indicates that the MIS sensor is quite stable at a wide temperature range. Furtherly, the relative resistance variation of the MIS sensor under different strains (0, 20, and 50% strains) is also tested at the temperature range of 30–40 °C. The resulted resistance change ($\Delta R/R_0$) decreases with the increase of temperature, demonstrating that the MIS sensor is an appropriate candidate as stretchable temperature sensor (Fig. S12i).
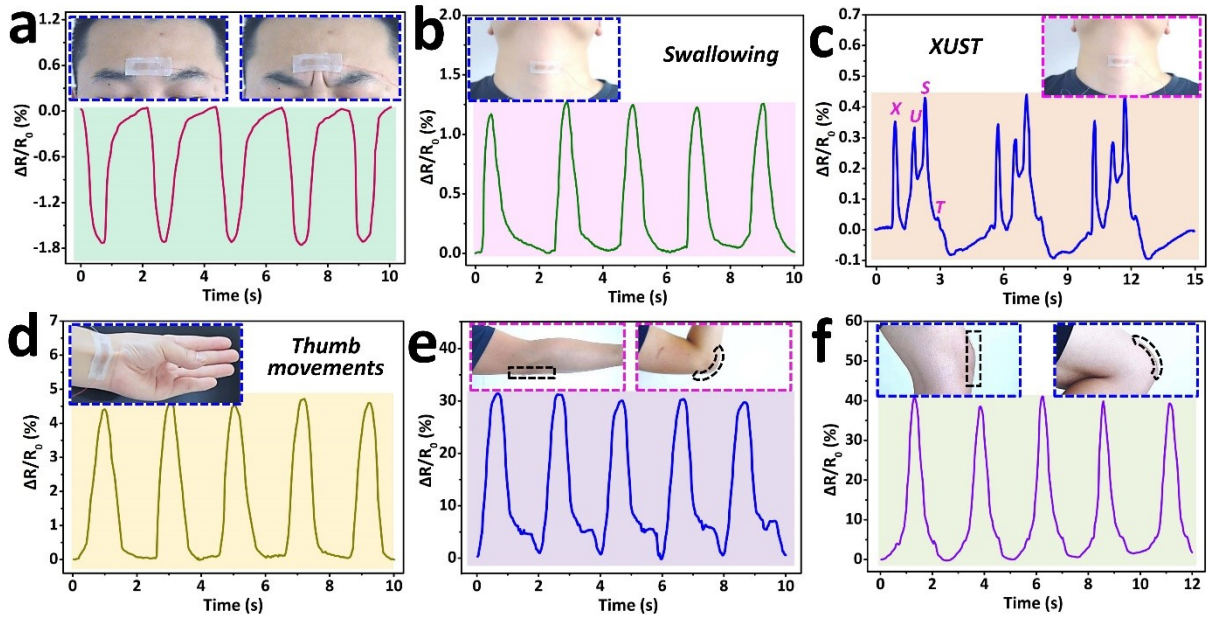
Fig. S13 (a-f) Relative resistance changes of the MIS sensor when it is attached to the eyebrows, throat, wrest joint, elbow join, and knee joint to sense the movements such as frowning (a), swallowing (b), speaking (c), and thumb movements (d), elbow bending (e), and knee bending (f), respectively.
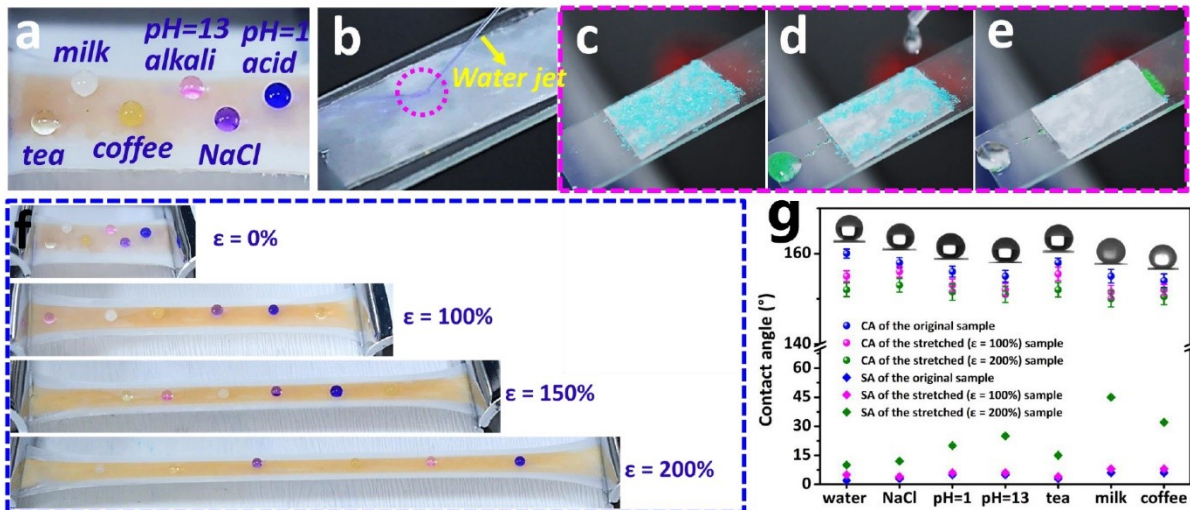
Fig. S14 (a) Optical image demonstrates the surface liquid wettability of the MIS sensor. (b-e) Water repellency (b) and self-cleaning property (c-e) of the superhydrophobic VHB substrate' surfaces. (f) Surface wettability of the MIS sensor when exposing to different extents of linear stretching from 0% to 200%. (g) Variations of the contact angles (CAs) and the sliding angles (SAs) of the MIS sensor surface to different liquid droplets when the sensor is exposed to different extents of linear stretching including 0%, 100%, 200%.

Water repellency is particularly important for electronics in practical application especially at water or humid environment. Herein, in light of the excellent superhydrophobicity of the top VHB layer, the obtained MIS sensor shows excellent repellency to various liquids droplets (Fig. S14a) including milk, alkaline solution (pH = 13), acid solution (pH = 1), tea, coffee, and NaCl solution. Moreover, the top superwettable VHB layer shows extreme water repellency, a jet of water impacting the surface can completely bounce off without leaving any trace (Fig. S14b). Additionally, the contaminants on the superwettable VHB surface can be easily removed by the rolling water droplets, demonstrating favorable self-cleaning ability (Fig. S14c-e). For a typical MIS sensor, the water repellency should be preserved covering the working ranges of different stretching statuses. Under different degrees of stretching strains from 0% to 200%, the liquids droplets (as mentioned in Fig. S14a) always maintain the spherical shapes, indicating the surface of the MIS sensor remains favorable hydrophobicity (Fig. S14f). Furthermore, the detailed variations of the droplet wettability of the sensor under different tensile strains are shown in Fig. S14g. It can be observed that when the MIS sensor is stretched to different strains ($\varepsilon = 0 \sim 200\%$), the values of CAs slightly decrease while the SAs values increase due to the decrease of surface roughness of the top superwettable VHB layer under tensile strain. Nonetheless, the surface of the MIS sensor remains favorable hydrophobicity. It is thus concluded that the superhydrophobicity of the MIS sensor can be maintained during the stretching operation and sensing process.
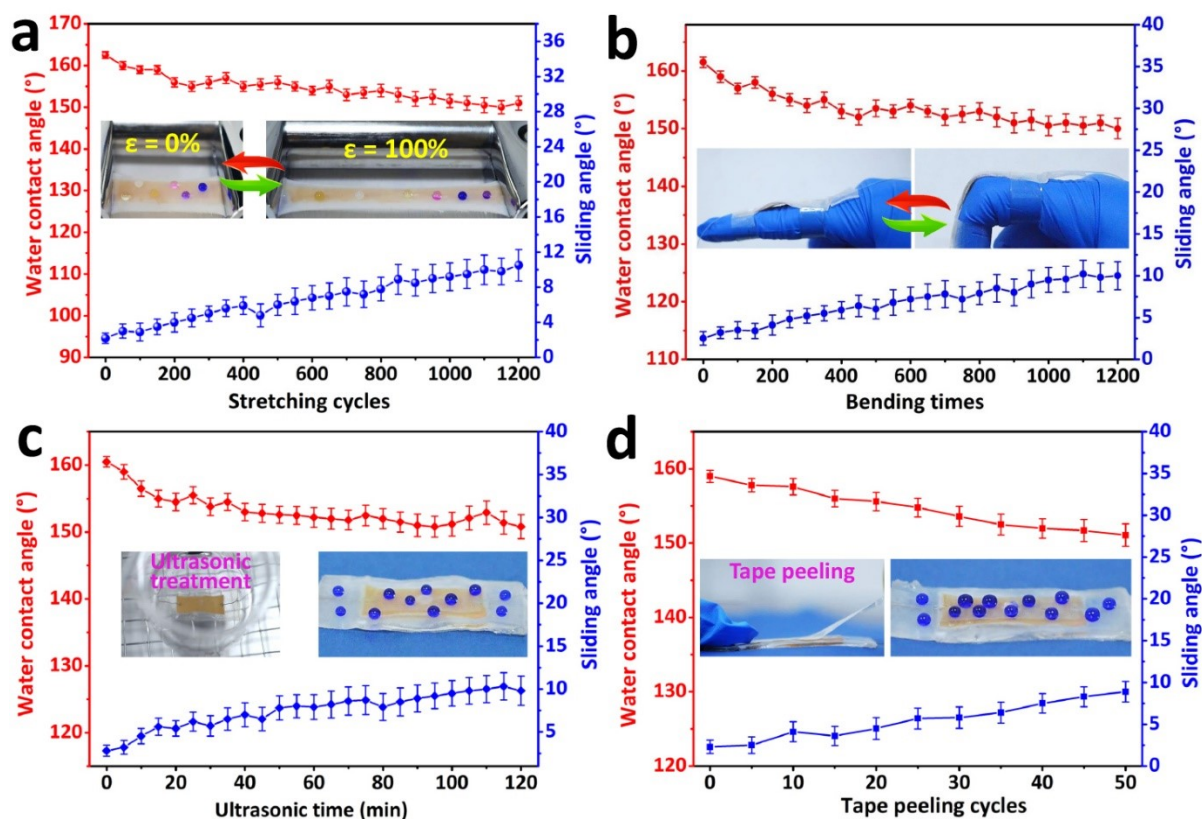
Fig. S15 (a-d) Surface wettability variations as the MIS sensor is exposed to cyclic stretching tests (a), cyclic bending tests (b), ultrasonic treatment in ethanol (c), and cyclic tape peeling tests (d), respectively.

Wettability durability is an important request for the MIS sensor to be applied in practice for a long service time. On this basis, the MIS sensor is further subjected to various tests to evaluate the stability of water repellency on its surface. As shown in Fig. S15a, the MIS sensor is exposed to periodically stretching (100%) and releasing tests, where the CA and SA of the sensor surface are measured after every 50 cycles. It can be found that, even after being cyclically stretched for 1200 times, the sample maintains a CA ~ 151.2° and a SA ~ 9.5°, revealing the potential for long-term use without decay of superhydrophobicity. Owing to the flexibility, the MIS sensor can be firmly attached onto the finger of a volunteer (Fig. S15b) for cyclic bending test. As expected, after 1200 bending cycles, the MIS sensor remains stable water repellency and low roll-off angle. In addition, we also investigate the stability of the

surface superhydrophobicity of the MIS sensor when exposing to ultrasonication treatment and adhesive tape peeling tests, respectively. It can be noted in Fig. S15c and d that even after 120 minutes ultrasonic treatment and 50 cycles tape peeling tests, the corresponding MIS sensors still maintain favorable water repellency with a CA greater than 150° and a roll-off angle lower than 10°, demonstrating favorable wettability durability.
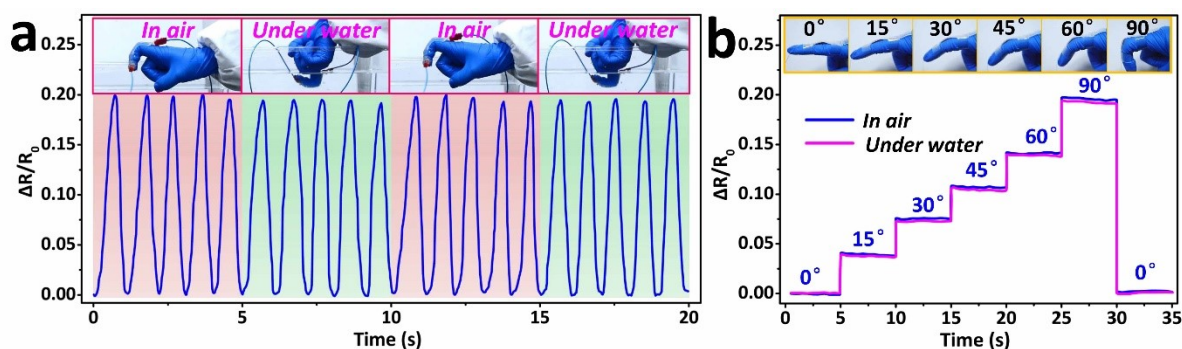
Fig. S16 (a) Relative resistance variations when the finger attached with the MIS sensor repeatedly bending and releasing in air and underwater environments. (b) Relative resistance variation responses of the MIS sensor to different finger bending angles in air and underwater conditions.

To further investigate the underwater wearable application performance of the MIS sensor, we attach the sensor to the finger of a volunteer and compare the signals when the sensor works in the air and underwater. Notably, the results in Fig. S16a and Video S6 indicate that the relative electrical variation in these two different environments is almost identical, confirming the possibility of the MIS sensor for reliable underwater applications. When the finger attached with the MIS sensor is completely immersed in water, the bending of the

finger results in resistance change with favorable recoverability. Such potential of underwater application is attributed to the good encapsulation and superhydrophobicity of the MIS sensor as discussed earlier. Moreover, the bending duration and bending angle of the finger can also be well recognized during the above testing process. As shown in Fig. S16b, with the increasing of the finger bending angle (0°–90°), the relative resistance of the MIS gradually increases, and such variation is basically consistent in both air and underwater environments. These results reveal the potential of the MIS sensor for real-time monitoring of the body motion underwater.

Table S1 Comparison of the main parameters of ionogel-based strain sensors in this work and pervious mainstream works

Component	Mechanical property		Strain Sensor		Ref.
	Tensile strain (%)	Tensile stress (MPa)	Detection strain range (%)	Gauge Factor (GF)	
WPU/mHNTs-ILs	1096	2.09	0.1 ~ 400	1.28 (0.1% ~100%)	This work
				2.13 (100% ~ 400%)	
PU/ILs	310%	1.8	0.1 ~ 200	1.53 (0.1% ~ 50%)	1
				2.14 (50% ~ 200%)	
PU-ILs	327%	1.56	0.1 ~ 300	1.23 (0.1% ~ 50%)	2
				1.54 (50% ~ 300%)	
PAAm/PAA-Fe^{3+}/ NaCl	537.5	1.18	0.2~ 500	1.23 (0.1% ~ 200%)	3
				1.96 (200% ~ 500%)	
PAA-TA@CNC-Al^+	2600	0.25	0 ~ 2000	0.23 (0 ~ 40)	4
				0.76 (40 ~ 65)	
				4.9 (65 ~ 75)	
NaCl/SA/PAA	1480	0.27	0 ~ 1000	0.65 (0 ~ 10)	5
				3.03 (10 ~ 1000)	

PVA/PVP/IL$_2$	821	7.7	0 ~ 800	1.01 (0 ~ 200) 1.85 (200 ~ 800)	6
F127DA-PAA/ILs	862	0.032	0 ~ 800	1.29 (0~400) 2.08 (400 ~ 800)	7
PEA/SiO$_2$/ILs	580	0.115	0 ~ 500	1.3 (0 ~ 100) 1.23 (100 ~ 250) 1.06 (250~500)	8
PAM-LiCl	300	~	0 ~ 300	0.7762	9
talc-PVA-AlCl$_3$	435	0.7	0 ~ 100	9.17 (0 ~ 1.2) 1.3 (1.2 ~ 100)	10
PDA@talc-PAM-KCl	1500	0.013	0 ~ 1000	0.125 (0 ~ 100) 0.693 (100 ~ 1000)	11
Agar/PAM-LiCl	1680	0.22	0 ~ 1100	0.5 (0 ~ 500) 1.8 (500 ~ 1000)	12
DN agar/AAC−Fe^{3+}	3174.3	0.068	0 ~ 1000	0.46 (0 ~ 100) 0.83 (100 ~ 1000)	13
Clay-OEGMA	~	~	0 ~ 600	0.4 (0 ~ 100) 2.23 (100 ~ 600)	14
agar/NaCl/PAM DN	1920	0.4	0~1600	0.7 (0 ~ 100) 2.1 (100 ~ 1600)	15
PVA/SA/NaCl/GL	582	1.19	0 ~ 582	1.3 (0 ~ 100) 2.0 (100 ~ 582)	16
PAAm-Gelatin DN	849	1.66	0 ~ 600	2.04	17
PAM/CMC/NaCl	1100	0.43	0 ~ 800	0.104 (0 ~ 300) 0.214 (300 ~ 800)	18
Laponite-AMPS/DAC-P (SBMA-HEMA)	2000	0.27	100	1.8	19
agar/AAC-FeCl$_3$	> 1000	~	0 ~ 650	1.66	20

Table S2 Sensing performance of the IL-based hybrid ionogels.

Material	Strain sensing performace		Stress sensing perfprmace	
	Detection strain range (%)	GF	Detection stress range (%)	S (KPa^{-1})
WPU/ILs (No surface micro structure)	1 ~ 400	0.46 (1 ~ 100) 1.03 (100 ~ 300) 2.02 (300 ~ 400)	0.1 ~ 12 KPa	0.26 (0.1 ~ 0.5) 0.15 (0.5 ~ 2) 0.006 (6 ~ 12)

WPU/mHNTs-ILs (No surface micro structure)	1 ~ 400	0.97 (1 ~ 100)	0.1 ~ 15 KPa	0.23 (0.1 ~ 3)
		1.35 (100 ~ 400)		0.01 (6 ~ 15)
WPU/mHNTs-ILs (MIS)	0.1 ~ 400	1.28 (0.1 ~ 100)	0.001 ~ 15 KPa	0.38 (0.001 ~ 3)
		2.13 (100 ~ 400)		0.05 (6 ~ 15)

References

1. J. Xu, H. Wang, X. Du, X. Cheng, Z. Du, H. Wang, *Chem. Eng. J.*, 2021, **426**, 130724

2. T. Li, Y. Wang, S. Li, X. Liu, J. Sun, *Adv. Mater.,* 2020, **32**, 2002706.

3. S. Li, H. Pan, Y. Wang, J. Sun, *J. Mater. Chem. A*, 2020, **8**, 3667−3675.

4. C. Shao, M. Wang, L. Meng, H. Chang, B. Wang, F. Xu, J. Yang, P. Wan, *Chem. Mater*., 2018, **30**, 3110−3121.

5. H. Huang, L. Han, X. Fu, Y. Wang, Z. Yang, L. Pan, M. Xu, *Adv. Funct. Mater.,* 2021, **31**, 2011176

6. D. Weng, F. Xu, X. Li, S. Li, Y. Li, J. Sun, *ACS Appl. Mater. Interfaces*, 2020, **12**, 57477–57485.

7. J. Lai, H. Zhou, Z. Jin, S. Li, H. Liu, X. Jin, C. Luo, A. Ma, W. Chen, *ACS Appl. Mater. Interfaces*, 2019, **11**, 26412−26420.

8. J. Wei, Y. Zheng, T. Chen, *Mater. Horiz.*, 2021, doi.org/10.1039/D1MH00998B.

9. G. Gu, H. P. Xu, S. Peng, L. Li, S. Chen, T. Lu, X. Guo, *Soft Robot.* 2019, **6**, 368−376.

10. X. Pan, Q. Wang, R. Guo, Y. Ni, K. Liu, X. Ouyang, L. Chen, L. Huang, S. Cao, M. Xie, *J. Mater. Chem. A*, 2019, **7**, 4525−4535.

11. X. Jing, H. Mi, Y. Lin, E. Enriquez, X. Peng, L. Turng, *ACS Appl. Mater. Interfaces*, 2018, **10**, 20897−20909.

12. B. Yang, W. Yuan, *ACS Appl. Mater. Interfaces,* 2019, **11**, 16765−16775.

13. F. He, X. You, H. Gong, Y. Yang, T. Bai, W. Wang, W. Guo, X. Liu, M. Ye, *ACS Appl. Mater. Interfaces*, 2020, **12**, 6442−6450.

14. H. Li, H. Zheng, Y. Tan, S. B. Tor, K. Zhou, *ACS Appl. Mater. Interfaces*, 2021, **13**, 12814−12823.

15. W. Hou, N. Sheng, X. Zhang, Z. Luan, P. Qi, M. Lin, Y. Tan, Y. Xia, Y. Li, K. Sui, *Carbohyd. Polym.*, 2019, **211**, 322−328.

16. H. Chen, Y. Gao, X. Ren, G. Gao, *Carbohyd. Polym.*, 2020, **235**, 116018.

17. X. Sun, F. Yao, C. Wang, Z. Qin, H. Zhang, Q. Yu, H. Zhang, X. Dong, Y. Wei, J. Li, *Macromol. Rapid Comm.*, 2020, **41**, 2000185.

18. Y. Liu, W. Cao, M. Ma, P. Wan, *Carbohyd. Polym.*, 2020, **248**, 116797.

19. L. Wang, G. Gao, Y. Zhou, T. Xu, J. Chen, R. Wang, R. Zhang, J. Fu, *ACS Appl. Mater. Interfaces*, 2019, **11**, 3506−3515.

20. H. Zheng, N. Lin, Y. He, B. Zuo, *ACS Appl. Mater. Interfaces,* 2021, **13**, 40013−40031.

21. S. Feng, Q. Li, S. Wang, B. Wang, Y. Hou, T. Zhang, *ACS Appl. Mater. Interfaces,* 2019, **11**, 21049−21057.

22. F. Wang, S. Zhang, Y. Zhang, Q. Lin, Y. Chen, D. Zhu, L. Sun, T. Chen, *Nanomaterials,* 2019, **9**, 343.

23. H. Ota, K. Chen, Y. Lin, D. Kiriya, H. Shiraki, Z. Yu, T. J. Ha, A. Javey, *Nat. Commun.*, 2014, **5**, 5032.

24. Y. S. Ye, J. Rick, B. J. Hwang, *J. Mater. Chem. A,* 2013, **1**, 2719−2743.

25. N. Jiang, X. Chang, D. Hu, L. Chen, Y. Wang, J. Chen, Y. Zhu, *Chem. Eng. J.*, 2021, **424**, 130418.

26. D.-Y. Youn, U. Jung, M. Naqi, S.-J. Choi, M.-G. Lee, S. Lee, H.-J. Park, I.-D. Kim, S. Kim, *ACS Appl. Mater. Interfaces* 2018, **10**, 44678−44685.

Supplementary Videos

Video S1 shows the evolution of the relative resistance variation at different compression frequency under a pressure of 1.5 KPa. (MP4)

Video S2 and **Video S3** show the variations in relative resistance of the MIS sensors during continuous touching and moving away from hot (60 °C) and cool (25 °C) water process and continuous pressing and moving away from hot (60 °C) and cool (25 °C) water process, respectively. (MP4)

Video S4 shows the sensing performance of the MIS sensor to finger motions in both air and underwater environments. (MP4)

Video S5 and **Video S6** show the resistance variations of the MIS sensor in response to water droplets with different dropping frequency (The droplet falling height is set as 20 cm, and the size of each droplet is about 50 μL) and water waves with different motion frequency, respectively. (MP4)

Video S7 and **Video S8** show the resistance variations of the MIS sensor towards the constant and the different swing frequency of the "fish tail", respectively. (MP4)

Video S9 ~ Video S11 demonstrate the applications of the MIS sensor in controlling the warning lamp via its directly contact sensing performance, underwater non-contact sensing performance, and under saltwater non-contact sensing performance, respectively. (MP4)